Received: 5 March 2022 | Accepted: 21 June 2022

DOI: 10.1002/jmv.27958

RESEARCH ARTICLE

JOURNAL OF MEDICAL VIROLOGY WILEY

Molecular imaging on ACE2-dependent transocular infection of coronavirus

Danni Li[1] | Liyan Xiong[2] | Guixia Pan[1] | Tingfang Wang[2] | Rou Li[1] | Lizhi Zhu[1] | Qianqian Tong[1] | Qinqin Yang[1] | Ye Peng[1] | Changjing Zuo[1] | Cong Wang[3] | Xiao Li[1,4]

[1]Department of Nuclear Medicine, Shanghai Changhai Hospital, Shanghai, China

[2]School of Medicine, Shanghai University, Shanghai, China

[3]Department of Cardiology, Zhongshan Hospital, Shanghai Institute of Cardiovascular Diseases, Fudan University, Shanghai, China

[4]Shanghai Institute of Applied Physics, Chinese Academy of Sciences, Shanghai, China

Correspondence

Changjing Zuo, Department of Nuclear Medicine, Shanghai Changhai Hospital, Shanghai 200433, China.
Email: changjing.zuo@qq.com

Cong Wang, Department of Cardiology, Zhongshan Hospital, Shanghai Institute of Cardiovascular Diseases, Fudan University, Shanghai 200322, China.
Email: wang.cong1@zs-hospital.sh.cn

Xiao Li, Shanghai Institute of Applied Physics, Chinese Academy of Sciences, Shanghai 201800, China.
Email: lixiao_nm@smmu.edu.cn

Funding information

"Discipline Construction Climbing 234 Plan" of Changhai Hospital of Naval Medical University (Second Military Medical University), Grant/Award Number: 2019YPT002; 2020YPT002; Shanghai Sailing Program, Grant/Award Number: 18YF1404100; National Natural Science Foundation of China, Grant/Award Number: 81800349; Science and Technology Support Project in Biomedical Field of "Science and Technology Innovation Action Plan" of Shanghai Science and Technology Commission, Grant/Award Number: 21S21902100; Shanghai "Rising Stars of Medical Talent" Youth Development Program, Grant/Award Number: SHWRS(2020)_087

Abstract

A transocular infection has been proved as one of the main approaches that severe acute respiratory syndrome coronavirus 2 (SARS-CoV-2) invades the body, and angiotensin-converting enzyme 2 (ACE2) plays a key role in this procedure. Dynamic and quantitative details on virus distribution are lacking for virus prevention and drug design. In this study, a radiotraceable pseudovirus packed with an enhanced green fluorescent protein (EGFP) gene, ^{125}I-CoV, was prepared and inoculated in the unilateral eye of humanized ACE2 (hACE2) mice or ACE2-knockout (ACE2-KO) mice. Single-photon emission computed tomography/computed tomography images were acquired at multiple time points to exhibit ACE2-dependent procedures from invasion to clearance. Positron emission tomography (PET) and western blot were performed to quantify ACE2 expression and verify the factors affecting transocular infection. For the transocular infection of coronavirus (CoV), the renin–angiotensin–aldosterone system (RAAS), lungs, intestines, and genital glands were the main targeted organs. Due to the specific anchor to ACE2-expressed host cells, virus concentrations in genital glands, liver, and lungs ranked the top three most and stabilized at 3.75 ± 0.55, 3.30 ± 0.25, and 2.10 ± 0.55% inoculated dose (ID)/mL at 48 h post treatment. Meanwhile, ACE2-KO mice had already completed the in vivo clearance. In consideration of organ volumes, lungs (14.50 ± 3.75%ID) and liver (10.94 ± 0.71%ID) were the main in-store reservoirs of CoV. However, the inoculated eye (5.52 ± 1.85% ID for hACE2, 5.24 ± 1.45%ID for ACE2-KO, $p > 0.05$) and the adjacent brain exhibited ACE2-independent virus infection at the end of 72 h observation, and absolute amount of virus played a key role in host cell infection. These observations

Danni Li, Liyan Xiong, and Guixia Pan contributed equally to this study.

on CoV infection were further manifested by infection-driven intracellular EGFP expression. ACE2 PET revealed an infection-related systematic upregulation of ACE2 expression in the organs involved in RAAS (e.g., brain, lung, heart, liver, and kidney) and the organ that was of own local renin–angiotensin system (e.g., eye). Transocular infection of CoV is ACE2-dependent and constitutes the cause of disturbed ACE2 expression in the host. The brain, genital glands, and intestines were of the highest unit uptake, potentially accounting for the sequelae. Lungs and liver were of the highest absolute amount, closely related to the respiratory diffusion and in vivo duplication. ACE2 expression was upregulated in the short term after infection with CoV. These visual and quantitative results are helpful to fully understanding the transocular path of SARS-CoV-2 and other CoVs.

KEYWORDS
ACE2, coronavirus, infection, molecular imaging, SARS-CoV-2, transocular

1 | INTRODUCTION

Coronavirus disease 2019 (COVID-19) caused by severe acute respiratory syndrome coronavirus 2 (SARS-CoV-2) has become a global pandemic threat to people. The COVID-19 pandemic has prompted a lot of research on how the virus is transmitted in vivo.[1] In view of epidemic spread, prevention, and control of coronavirus, figuring out the path of in vivo transmission will be instructive to establish the specific prevention measures.

COVID-19 is primarily deemed as a disease of the respiratory system. Furthermore, the details of SARS-CoV-2 infection, including invasion, transmission in respiratory tracts, specific attachment to angiotensin-converting enzyme 2 (ACE2) of host cells, spike protein priming by cellular proteases transmembrane protease serine 2 (TMPRSS2), as well as intracellular duplication and release, have been widely reported.[2,3] In general, the specific binding of the spike protein of coronavirus to ACE2 protein is the principal factor in infecting host cells, especially as an extracellular domain binding force between SARS-CoV-2 and ACE2 is as low as 15 nM (10–20 times the force between SARS-CoV and ACE2).[4]

In addition to the upper respiratory tracts, the eyes were recognized as another organ for viruses to enter the body.[5] A recent case report described a clinician who was infected with SARS-CoV-2 while wearing an N95 mask but without eye protection. In addition, this physician presented symptoms of redness of the eyes already before the onset of pneumonia.[6] These findings implied that ocular symptoms might be the first sign of early SARS-CoV-2 infection. In addition, Zhou et al.[7] reported the susceptibility of the conjunctiva, which served as a portal of entry and a reservoir for viral transmission. On one hand, the ocular surface area was reported to be two orders of magnitude greater than for the nares and mouth, making it easy for respiratory droplets to be deposited.[8] For the exposed cornea with high ACE2 expression but without an effective way to block the interactions with the surroundings, respiratory droplets or particles from the air exhaled by an infected person, aerosols, and direct contact with virus-contaminated hands contribute to the probabilities of virus infection.[9,10] Furthermore, given the high stability and long survival time of viruses on the surface of the inanimate objects,[11] the indirect virus transmission from inanimate objects to humans carries a nonnegligible potential risk. On the other hand, in the clinic, visual conjunctivitis has been reported as an ocular manifestation of COVID-19, and tears have the potential to spread the infection by draining into the nasopharynx through the nasolacrimal system.[12]

Several research have confirmed that the basis of coronavirus infection was ACE2 and TMPRSS2 expression in the eyes, a compatible pathway with other ACE2-related organs, such as the lung, heart, and liver.[13] Before the breakout of COVID-19, the disorder ACE2 expression of eyes has been researched on glaucoma, uveitis, and diabetic retinopathy.[14–16] The diseased conjunctival tissue was of an upregulated ACE2 level, as well as the pharmacologic upregulation, further increased the susceptibility.[17–19] Actually, there is the microrenin–angiotensin system involved in regulating the dynamic changes of ACE2, so the upregulated ACE2 caused by glaucoma and other diseases further increased the risk of coronavirus infection.[20] Therefore, comprehending and controlling transocular viral infection help to cut off one of the main sources of coronavirus infection.

Different from the other organs with high ACE2 expression, the eyes are directly exposed to outside surroundings, leading to a more complex procedure of transocular infection, potentially involving lymph and blood circulation, permeation of the blood–brain barrier, and so on. Therefore, the transocular path of infectious coronaviruses, such as 1) how does the virus complete the distribution and clearance of internal organs, and 2) whether the transocular infection is heavily affected by ACE2 expression, should be figured out. In a methodological view, there is still a lack of dynamic and intuitive in vivo assessment methods in tracking coronavirus. In this study, the Iodine-125 labeled pseudovirus of SARS-CoV-2 packed with enhanced green fluorescent protein (EGFP) gene was developed to trace the transocular entry, the

specific distribution, and metabolic clearance process. Visual and quantitative assessment relying on single-photon emission computed tomography/computed tomography (SPECT/CT) and ACE2-positron emission tomography (PET) images will provide insights into the course of transocular infection of coronavirus and the relationship between ACE2 expression and coronavirus.

2 | METHODS

2.1 | Materials and model animals

SARS-CoV-2 spike pseudovirus (pSLenti-CMV-EGFP-3xFLAG-WPRE, Batch No. OP0812), composed of Spike envelope protein and mCherry/EGFP/Luciferase gene, was purchased from OBiO Technology Corp., Ltd., and all of the operations with pseudovirus were performed in a B2 type (100% external expelling) biological safety cabinet.

Iodine-125 was purchased from Shanghai XinKe Pharmaceutical Co., Ltd., and the related operations were performed in a host cell for synthesis.

This research was approved by the Ethics Committee of Shanghai University (Approval No.: ECSHU 2021-198 and ECSHU 2021-199). In order to fully exhibit ACE2-dependence, humanized ACE2 (hACE2) mice (C57BL/6J-Tgtn(CAG-human ACE2-IRES-Luciferase-WPRE-polyA) Smoc mice, SPF level) and ACE2-knockout (ACE2-KO) mice (C57BL/6J-*Ace2*^{em1Smoc} mice, SPF level) were used as "yes-or-no" biologic background on ACE2. These mice (12 weeks old, 25 g, male) were purchased from Shanghai Model Organisms Center and raised in clean level condition with a normal diet.

2.2 | Preparation of radiotraceable pseudovirus

Pseudovirus in 0.01 M phosphate-buffered saline (PBS) was kept at −40°C, and radiolabeled just before the in vitro or in vivo experiments, so as to keep the biological activity of enveloped spike protein and EGFP gene. Radioactive iodine was labeled via an indirect method. In detail, 185 MBq iodine-125 was first labeled to a tyrosine (Tyr) of 1 μg Bolton-Hunter reagent (*N*-hydroxysuccinimide [NHS]-Tyr) with iodogen as the catalyst, and free I-125 was removed with Sep-Pak QMA column. The obtained NHS-Tyr-^{125}I in saline then interacted with 5×10^6 TU pseudovirus at 4°C overnight. The unreacted NHS-Tyr-^{125}I was removed via centrifugal separation with a 10 000 ultrafiltration tube in a refrigerated centrifuge. The obtained SARS-CoV-2 ^{125}I-Tyr-spike pseudovirus (^{125}I-CoV) was suspended in saline. For each drop (10 μl) of ^{125}I-CoV suspension, 5×10^5 TU pseudovirus was contained with ca. 20 000 radioactive counts (quantified with SPECT scanner). For cell experiments, Iodine-125 was replaced by 'cold' iodine (iodine-127).

Radiochemical purity (RCP) of ^{125}I-CoV and in vitro stability in 0.01 M PBS was measured using a thin layer chromatography with radiodetector (radio-TLC) with saline as mobile phase and instant TLC-SG (glass microfiber chromatography paper impregnated with silica gel) as stationary phase. The stability of ^{125}I-CoV was further evaluated by the in vivo stability that was manifested by the thyroid uptake reflected in SPECT/CT images.

2.3 | In vitro testing on ACE2 targeting

Cell line HEK293T-ACE2 that overexpressed ACE2 protein was used as the model cells in evaluating the maintenance of infection ability of ^{127}I-CoV. 10^5 cells were coincubated with 10^5 TU pseudovirus or ^{127}I-CoV for 12 h, respectively, and then washed with 0.01 M PBS three times to remove the excess pseudovirus. Cells were incubated for another 72 h and then observed with a fluorescence microscope (NIB610-FL, NEXCOPE) at 395 nm excitation light. The infected HEK293T-ACE2 cells were dyed green due to the intracellular expression of the EGFP gene. The ratios of host cells with green fluorescent protein were quantified to compare the infection ability of pseudovirus before and after modification.

2.4 | SPECT/CT imaging on ^{125}I-CoV distribution

Mice, including hACE2 mice and ACE2-KO mice, were kept awake during the transocular inoculation, and 10μl suspension of ^{125}I-CoV was gently inoculated into the rim of the right eye, leaving the opposite eye without any treatment. Between the interval of SPECT/CT scans, mice were awake and fed with a normal diet, so as to realize the sufficient interaction between ^{125}I-CoV and cornea. The blank control group of hACE2 mice was transocular inoculated with Na^{125}I only. Considering that the half-life of ^{125}I in vivo is longer than that of the virus, the cutoff time point for SPECT/CT imaging was determined as follows: 1) radioactivity concentration in the thyroid was observed by SPECT/CT, indicating substantial dehalogenation; 2) the virus was almost cleared in vivo.

Mice were anesthetized with 75 μl 3% (wt/wt) pentobarbital sodium for SPECT/CT scans, which were performed at different time points (3, 6, 12, 24, 48, and 72 h post the treatment (P.T.) using SPECT/CT scanner (Symbia T16; Siemens) equipped with a low energy universal collimator. SPECT image acquisition parameters were set as follows: energy peak, 35 keV; window width, ±10%; matrix, 64 × 64; zoom, 1.78; time length of each slice, the 30 s for the first 24 h and 60 s for the rest time points. CT image acquisition parameters were set as follows: tube voltage, 130 kV; tube current, 35 mA; and slice thickness, 1 mm. After the acquisition was finished, coregistration of SPECT and CT images was performed, and slight drag in three-dimensional (3D) view was carried out to correct the position moving during the scans.

2.5 | 3D reconstruction and semiquantification

3D SPECT/CT images were fusions of volume-rendered technique-derived 3D CT images in soft tissue view and cross-sectional SPECT images. In detail, CT data were loaded in 3D view, and SPECT data

were fused to CT in 3D fusion mode. The fused 3D SPECT/CT images were read in free view mode, and the needless images of extracorporeal things were sketched and incised in volumes of interest (VOIs) Punch mode.

Semi-quantification of ^{125}I-CoV distribution was performed in the volumetric activity module. In the fused SPECT/CT images, regions of interest (ROIs) were drawn in multiple-continuous transverse slices, so as to quantify the involved radioactive counts and interested volume. Some ACE2-related organs, such as spleen and pancreas thymus glands, were not analyzed, due to the difficulty in drawing ROIs of relatively small volume. Additionally, some urethral canal was inevitably involved in VOIs of genital glands, because of the compact physiological structures. Hence, the dynamic changes of specific uptake of the inoculated eye, the adjacent brain, renin–angiotensin–aldosterone system (RAAS) organs, including heart, liver, and kidneys, and specific uptake of other organs with relatively high ACE2 expression, including lungs, intestinal tracts, and genital glands, were manually outlined and quantified based on the VOIs. The outlined VOIs were double-checked by another radiologist. For each interesting organ, the percentage of inoculated dose per milliliter (%ID/mL) and the percentage of inoculated dose (%ID) were measured.

2.6 | PET imaging on ACE2 expression

ACE2 PET was utilized to characterize the in vivo ACE2 expression before and after the inoculation with ^{125}I-CoV. Mice were anesthetized and intravenously injected with 7.4 MBq ACE2-targeted ^{68}Ga-cyc-DX600 (RCP ≥ 95%, prepared in-house according to our reported method[21]). PET/CT images were acquired at 60 min postinjection using PET/CT scanner (Biograph 64; Siemens). Scans started with a low-dose CT scan followed by a PET scan. The image acquisition parameters were set as follows: for CT, tube voltage: 120 kV; tube current: 35 mA; pitch: 1.0; reconstructed layer thickness: 1 mm; for PET, acquisition of whole-body images for each bed was 3 min.

The postprocessing workstation TureD system was utilized for image reconstruction to form maximum intensity projection images. In the retrospective analysis of ACE2 PET/CT images, ROIs were manually drawn on the infected organs reflected in ^{125}I-CoV SPECT/CT images, and PET/CT workstation provided a quantification value of tracer uptake as a standardized uptake value (SUV). For ACE2 expression, SUV_{ACE2} was defined as the difference value of SUV_{max} of ROIs in corresponding hACE2 mice and ACE2-KO mice, where the latter value stands for the nonspecific distribution of ^{68}Ga-cyc-DX600.

2.7 | Western blotting on ACE2

After 72 h of inoculations with ^{125}I-CoV, mice were raised for another 2 days, so as to guarantee the intracellular EGFP gene expression. Mice were killed with an overdose of anesthesia. Fresh tissues from hACE2 and ACE2-KO mice, including heart, liver, kidneys, lungs, small intestines, genital glands, eyes, and brain, were lysed in radioimmunoprecipitation assay buffer containing 1 mM phenylmethylsulfonyl fluoride, respectively. After removal of cell debris by centrifugation (11 000 rpm, 4°C, 10 min), the supernatant protein solution was adjusted to equal concentration by the bicinchoninic acid protein determination method and then mixed with loading buffer. Samples were resolved by sodium dodecyl sulfate-polyacrylamide gel electrophoresis and transferred to nitrocellulose membranes, blocked with 5% milk in TBST. Proteins were probed with an anti-ACE2 antibody (Abcam; ab108209) overnight at 4°C. The membranes were washed three times with TBST, incubated with horseradish peroxidase-conjugated secondary antibody for 1 h at room temperature, and washed three times again with TBST. Signals were detected by enhanced chemiluminescence.

2.8 | Ex vivo fluorescence imaging on EGFP

To verify the observations on coronavirus distribution, EGFP expression resulting from the inoculation with SARS-CoV-2 spike pseudovirus was measured. The isolated eyes and brain were imaged with optical/fluorescent imager (InVivo Smart-LF; Vieworks Co., Ltd.) with GFP mode: excitation at 390–490 nm for 1 s and emission at 500–550 nm.

2.9 | Statistics

In this study, the values of organ-specific uptake and SUV_{ACE2} were presented as mean ± standard deviation. The paired-samples *t*-test was used to compare the difference between hACE2 mice and ACE2-KO mice. The difference with a $p < 0.05$ was set as statistical significance. Figures 2A,B, 3D, 5, 6A,B, and 8 were drawn with Origin 8, and Figures 7B,E were drawn with SPSS statistics 26.

3 | RESULTS

3.1 | Preparation of ^{125}I-CoV and in vitro test on ACE2 targeting

As shown in Figure 1, the radioactive iodine-125 was labeled as pseudovirus in a method with less impact on virus structure. I-125 was labeled to Bolton-hunter reagent with a labeling rate of 78.5 ± 3.5%. After purification with the QMA column, NHS-Tyr-^{125}I was further conjugated to the terminal amino groups of spike protein on the pseudovirus surface. The labeling yield of the final product was 35.1 ± 2.5%. As shown in Figure 2A, radio-TLC proved the RCP of purified ^{125}I-CoV was nearly 100%, and RCPs were > 95% during the 72 h preservation in 0.01 M PBS at 4°C. Additionally, no abnormal uptake resulting from de-labeling was observed in thyroids. So, the in vitro and in vivo stability of ^{125}I-CoV met the requirements for tracing pseudovirus.

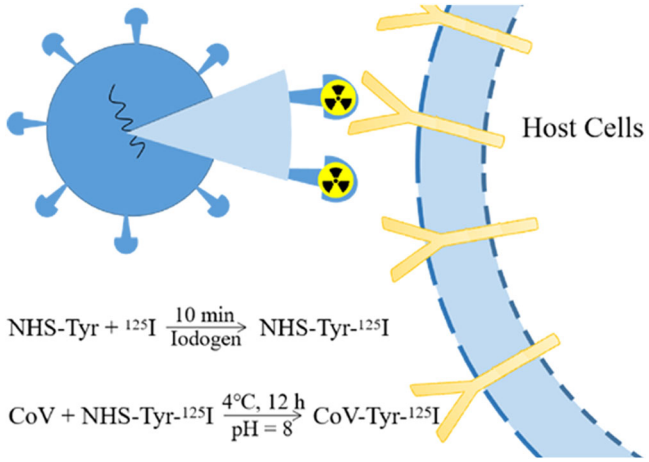

FIGURE 1 The schematic procedure of I-125 labeling to pseudovirus, and the specific attachment to ACE2-expressed host cells. ACE2, angiotensin-converting enzyme; CoV, coronavirus; NHS, *N*-hydroxysuccinimide; Tyr, tyrosinase.

As shown in Figure 2B–D, I-125 labeling did not affect the ability of the virus to specifically target ACE2. After coincubation for 3 days, there was no statistically difference in the ratio of EGFP-expressed cells (25.1 ± 3.1% for CoV and 26.9 ± 4.1% for ^{127}I-CoV, $p > 0.05$). Therefore, iodine-labeled pseudovirus can mimic the ahead steps of infection, including specific attachment to ACE2 protein, ACE2-mediated entrance to host cells, and intracellular RNA expression, rather than the intracellular duplication.

3.2 | In vivo metabolism of ^{125}I-CoV

3D SPECT/CT images exhibited ACE2-dependent procedures from invasion to clearance. As shown in Figure 3A,B, radiotraceable pseudovirus,^{125}I-CoV, was inoculated in the right eye, but the opposite eye was involved very little in the whole procedure of virus infection during the 72 h observation. The in vivo metabolism of free ^{125}I (i.e., Na^{125}I) and ^{125}I-CoV in hACE2 mice were completely

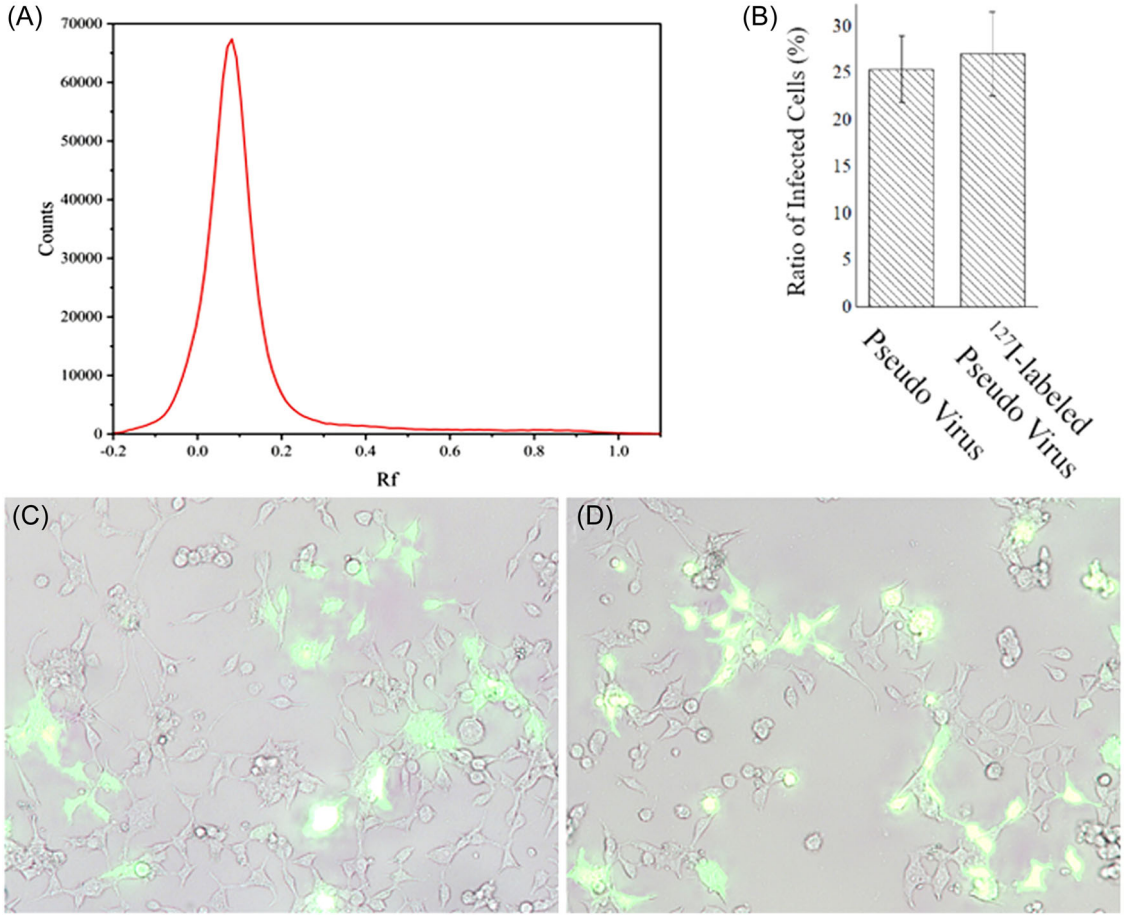

FIGURE 2 Characteristics of I-125 labeling to pseudovirus, including the radiochemical purity of purified ^{125}I-CoV (A), the transfection efficiency of EGFP gene to ACE2-expressed HEK293T cells (B), and the typical fused images of optical and fluorescence images of HEK293T cells incubated with pseudovirus (C) or ^{127}I-CoV (D). ACE2, angiotensin-converting enzyme; CoV, coronavirus; EGFP, enhanced green fluorescent protein.

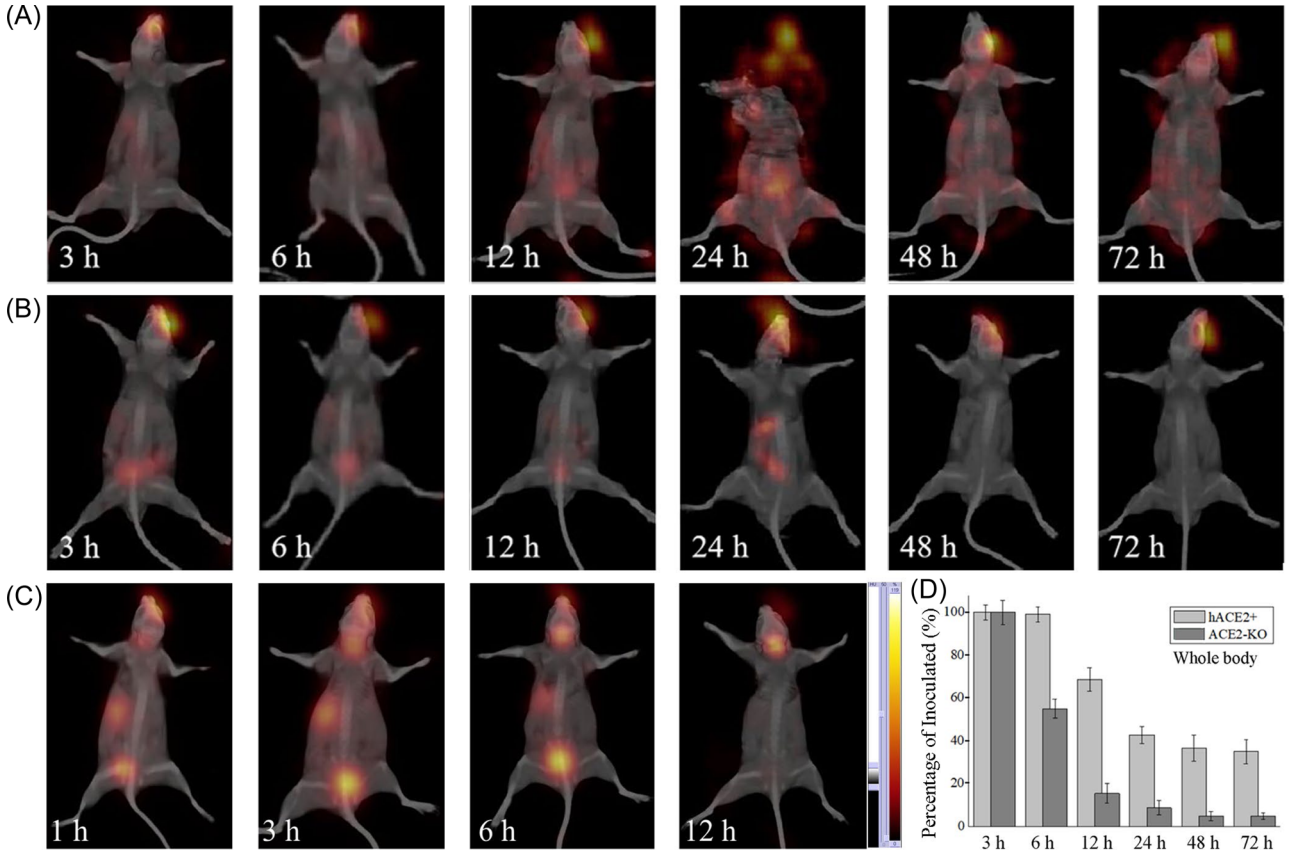

FIGURE 3 ACE2-dependent metabolism of transocular pseudovirus, including the dynamic 3D SPECT/CT images (in soft tissue view) of ACE2-dependent pseudovirus distribution for hACE2 mice ($n = 6$) (A) and ACE2-KO mice ($n = 3$) (B). (C) The metabolism pattern of $Na^{125}I$ in hACE2 mice ($n = 3$). (D) The quantitative information of whole-body metabolism. 3D, three dimensional; ACE2, angiotensin-converting enzyme; hACE2, humanized ACE2; KO, knockout; SPECT/CT, single-photon emission computed tomography/computed tomography.

different in rate and pattern. As shown in Figure 3C, an increasing radioactivity accumulation of free ^{125}I was found in the thyroid of the hACE2 mouse over time, and free ^{125}I faded from the inoculated eye and was then eliminated by the urinary system.

The in vivo metabolism of ^{125}I-CoV was totally different between hACE2 mice and ACE2-KO mice. As shown in Figure 3A (hACE2 mice) and Figure 3B (ACE2-KO mice), an obviously quicker metabolic clearance rate for ACE2-KO mice was recorded, while the real-time obvious bladder burden may be earlier than the first scanning time point. Correspondingly, the obvious radioactive signal in the bladder first appeared at 12 h P.T. for hACE2 mice. Intestinal excretion was another metabolic way, and a remarkable difference was observed between hACE2 mice and ACE2-KO mice. For ACE2-KO mice, a rice-shaped signal related to feces was observed; but for hACE2 mice, a diffused signal in enterocoelia related to ACE2 expression of intestinal tracts was observed. As a whole, more than 24 h were needed for in vivo clearance of transocular invaded ^{125}I-CoV, and ACE2 further postpone the metabolic clearance.

According to the quantitative information on whole-body metabolism in Figure 3D, the difference of residuals in the body between hACE2 and ACE2-KO mice was first detected at 6 h P.T., and the degree of difference tended to be stable at 48 h P.T. At this time point, the clearance of ^{125}I-CoV in ACE2-KO mice was completed with 5.06 ± 1.39%ID residuals (mainly in the inoculated eye). Accordingly, ACE2-specific binding of ^{125}I-CoV was completed as well with 36.68 ± 4.26%ID residuals (mainly in the inoculated eye, respiratory tracts, and enterocoelia). The residual radioactivity of hACE2 mice was stable since 48 h P.T., indicating that ^{125}I-CoV has been transferred into the host cells, where the steps of infection proceed to the intracellular gene expression.

3.3 | Organ-specific distribution of ^{125}I-CoV

For the transocular infection, RAAS, lungs, intestines, and genital glands were the main observed targets of coronavirus. On the basis of Figure 3D, ^{125}I-CoV was almost cleared from ACE2-KO mice at 12 h P.T.; ACE2-specific uptake and nonspecific distribution were stabilized at 48 h P.T. Therefore, cross-sectional images of the main observed organs of hACE2 and ACE2-KO mice with more details at these two time points were provided in Figure 4. Correspondingly, a quantitative analysis of the time-dependence of organ-specific metabolic curves was summarized in Figure 5. The other ACE2-related organs, such as the pancreas and spleen, were also potentially infected, but too small to be outlined in SPECT/CT images.

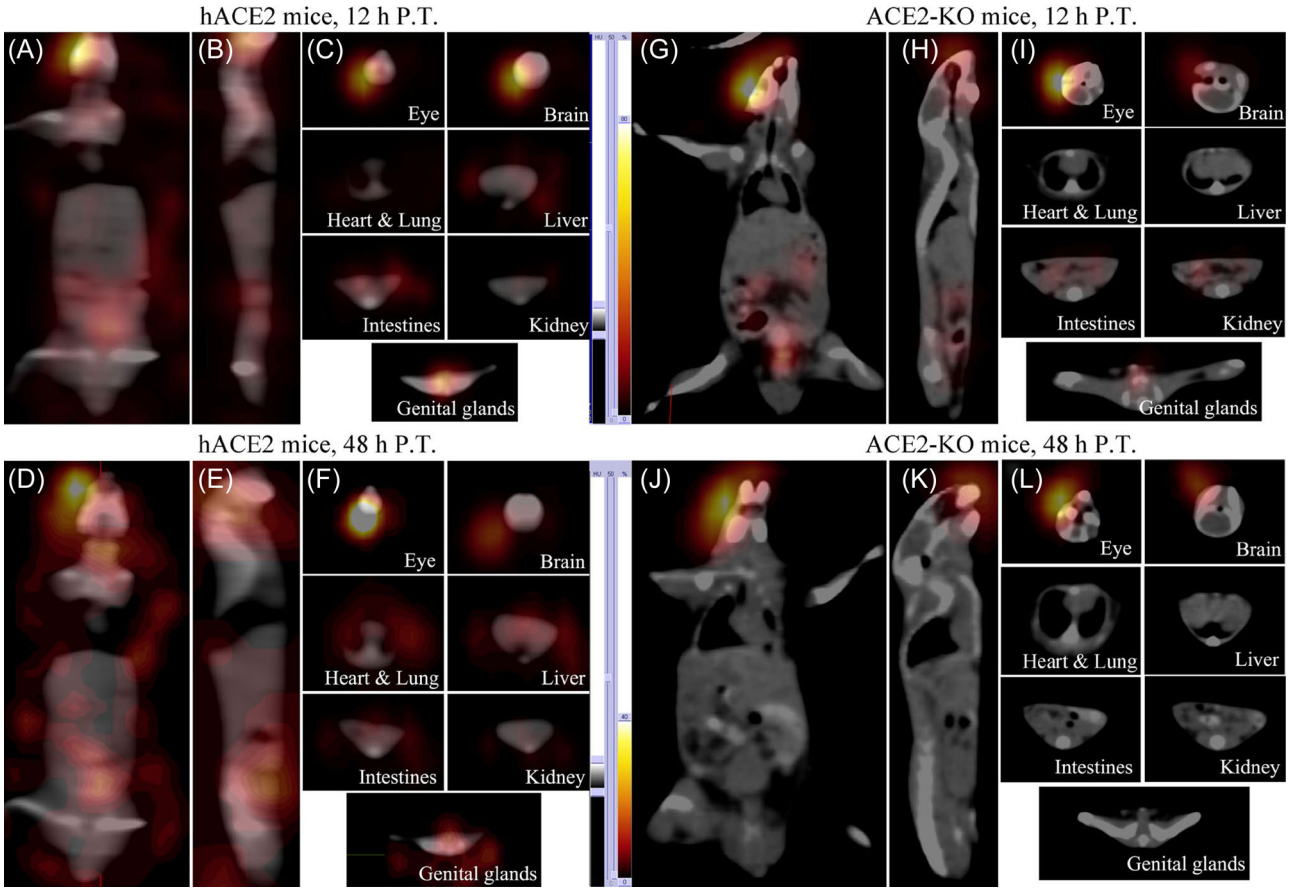

FIGURE 4 ^{125}I-CoV SPECT/CT images of hACE2 mice and ACE2-KO mice. For 12 h P.T., (A) the coronal section that included multiple organs, (B) the sagittal section that included brain, lung, liver, intestines, and genital glands, and (C) showed the transverse sections specific to eyes, brain, lungs, and heart (in one slice), liver, intestines, kidneys, and genital glands. For 48 h P.T., (D–F) showed the corresponding positions with a narrowed radioactivity range of SPECT images; (G–I) showed the corresponding images of ACE2-KO mice at 12 h P.T., and (J–L) images at 48 h P.T. ACE2, angiotensin-converting enzyme; hACE2, humanized ACE2; KO, knockout; P.T., post the treatment; SPECT/CT, single-photon emission computed tomography/computed tomography.

For RAAS organs of hACE2 mice, the specific uptake of the heart and kidney were influenced by the blood system and urinary system, respectively. The significant decreases in heart and kidney from 48 to 72 h P.T. lead to the simultaneously slight increases of the lung, intestinal tracts, and genital glands, potentially resulting from the wash away of ^{125}I-CoV that cannot complete the transmembrane. As the main organ to expel external substances, the liver was of the highest unit uptake of 3.10 ± 0.20%ID/mlL at 72 h P.T.

For the other ACE2-related organs, due to the specific anchor to ACE2-expressed host cells, virus concentrations of lungs, intestines, and genital glands of hACE2 mice stabilized at 2.10 ± 0.55, 0.50 ± 0.12, and 3.75 ± 0.55%ID/mL at 48 h P.T. Correspondingly, ACE2-KO mice have already completed the in vivo clearance at this time point. For lungs, specific uptake was quickly completed at 6 h P.T., and a fluctuation was observed due to the entrance into the blood circulation of ^{125}I-CoV.

For metabolic organs of all mice, such as kidneys, intestinal tracts, and liver, a rise-fall metabolic curve was observed. Meantime, for hACE2 mice, an ACE2-related delay of "rise-fall" turning point was observed when compared with ACE2-KO mice. The intestinal tracts and genital glands shared a similar trend in metabolism, but the quantification of genital glands was potentially influenced by urine signals during the early period. Additionally, urinary system-related genital glands (potentially affected by urine) were more quickly to reach stabilization than digestive system-related intestinal tracts.

Overall, virus concentrations in genital glands, liver, and lungs ranked the top three most and stabilized at 3.75 ± 0.55, 3.30 ± 0.25, and 2.10 ± 0.55%ID/mL at 48 h P.T., respectively. At the end of observation (72 h), genital glands were of the highest unit uptake 4.65 ± 0.75%ID/mL, and lungs were also of a relatively high unit uptake 2.90 ± 0.75%ID/mL, proving an infection potential in the transocular way. Figure 5H showed the parallel comparison of main organs outlined in SPECT/CT images of hACE2 mice, and these organ-specific infections formed the basis of symptoms of COVID-19. Notably, although the genital glands and the eye-adjacent brain (Figure 5H) were of the highest unit uptake, lungs (14.50 ± 3.75%ID) and liver (10.94 ± 0.71%ID) were the main

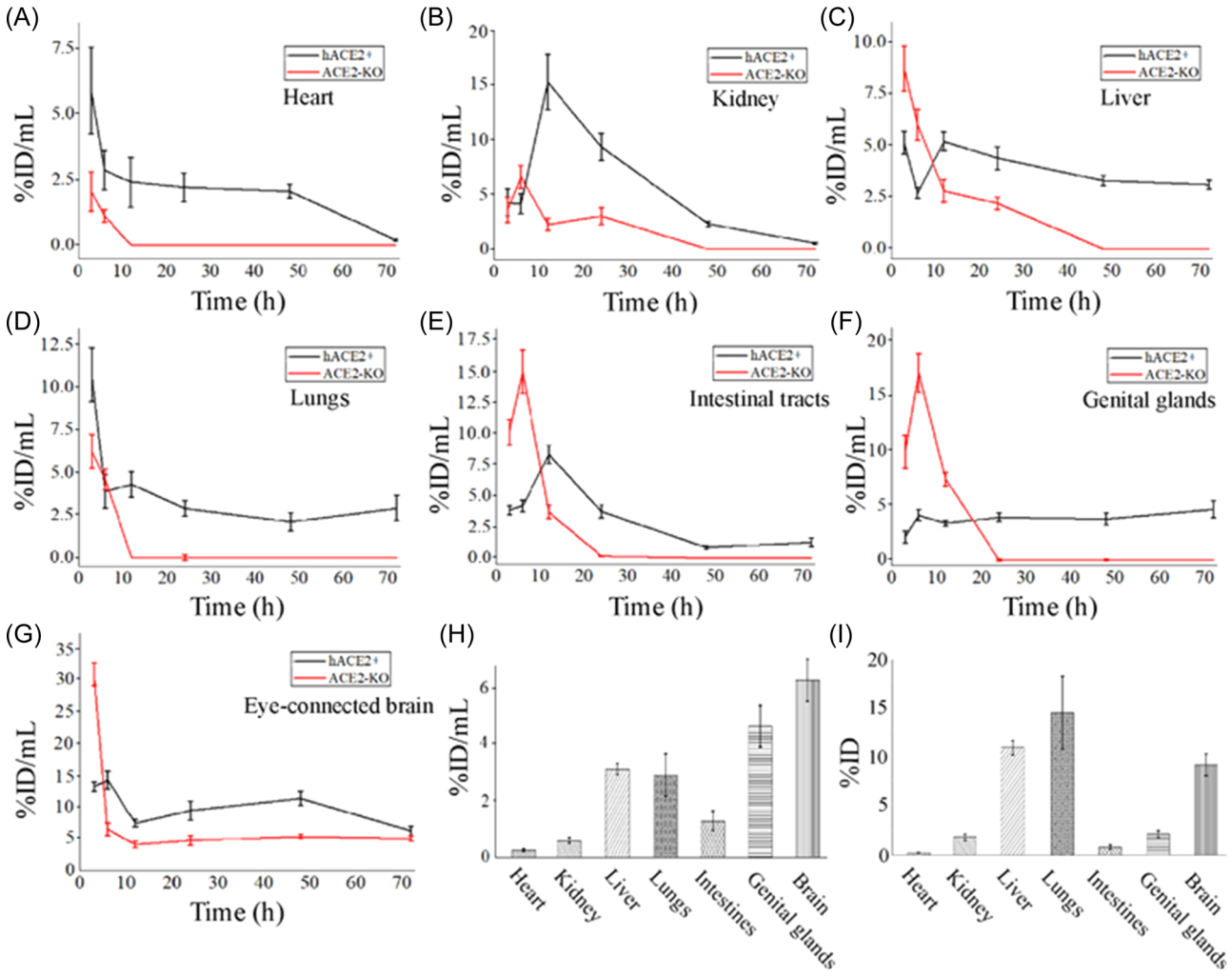

FIGURE 5 Specific uptake of RAAS organs (means ± SD, $n = 3$), including heart (A), kidney (B), and liver (C), and specific uptake of other organs with relatively high ACE2 expression, including lung (D), intestinal tracts (E), and genital glands (F); (G) showed the metabolic curve of the eye-adjacent brain; (H) summarized the unit volume uptake of these organs at 72 h P.T.; and (I) showed the organ-specific quantitative accumulation at 72 h P.T. ACE2, angiotensin-converting enzyme; hACE2, humanized ACE2; KO, knockout; P.T., post the treatment; RAAS, renin–angiotensin–aldosterone system.

in-store reservoirs for coronavirus spillover and diffusion in consideration of organ volumes (Figure 5I).

For the quantification of the radioactivity of inoculated eyes (Figure 6A), there was a similar tendency with the whole-body metabolism for hACE2 and ACE2-KO mice. However, the inoculated eye exhibited an ACE2-independent virus infection model at the end of observation. There was a statistical difference for the previous 48 h, but no statistical difference was observed at 72 h P.T. (5.52 ± 1.85%ID for hACE2, 5.24 ± 1.45%ID for ACE2-KO, $p > 0.05$). As shown in the virus quantification of the brain (Figure 6B), the metabolic rate of ^{125}I-CoV in the brain of hACE2 mice was more complex with a "fall-rise-fall" fluctuation that resulted from the direct reaction with coronavirus and the secondary targeted distribution from in vivo circulation. ACE2 expression of hACE2 mice resulted in a slight but significantly higher virus load than that of ACE2-KO mice at the end of observation. Additionally, despite the existence of a significant difference in ACE2 expression in the eyes and brain of hACE2 and ACE2-KO mice (Figure 6C), EGFP expression was comparable (Figure 6D). For the infection originated from the transocular path, the eyes were proved as the in-store reservoir for coronavirus spillover and diffusion to some extent.

3.4 | PET imaging and Western blotting on ACE2 expression

Figure 7A was the western blot of hACE2 mice and ACE2-KO mice, and the organ-specific uptake of ^{125}I-CoV significantly related to ACE2 expression of hACE2 mice as follows:

$$\text{Unit uptake of } {}^{125}\text{I} - \text{CoV} = 0.1 + 3.33 \times \text{Relative Intensity of ACE2 WB.}$$

$R^2 = 0.435$, $p < 0.05$ (Figure 7B). Additionally, western blot results of the above organs from ACE2-KO mice were of low or no ACE2 expression, and the total clearance of pseudovirus further proved the

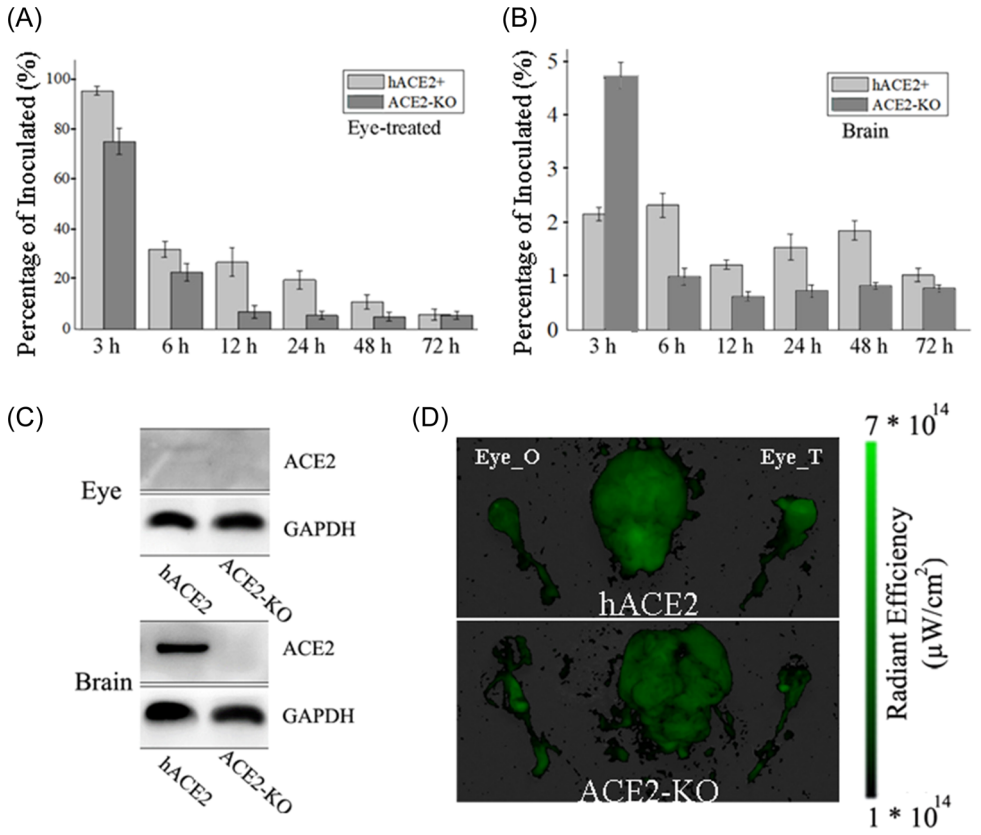

FIGURE 6 Quantitative information on the metabolism of the inoculated eye (A) and brain (B); Western blot of ACE2 expression in the eyes and brain of hACE2 mice and ACE2-KO mice (C); and fluorescence images of EGFP expressions in eyes and brain of hACE2 and ACE2-KO mice at 5 days P.T. (D) ($n = 3$, T: treatment; O: opposite). ACE2, angiotensin-converting enzyme; EGFP, enhanced green fluorescent protein; hACE2, humanized ACE2; KO, knockout; P.T., post the treatment.

ACE2-related uptakes. Hence, ACE2 expression was the main factor in coronavirus infection of visceral organs.

Figure 7C,D was the ACE2 PET of hACE2 and ACE2-KO mice. SUV_{ACE2} of ACE2 PET using ^{68}Ga-cyc-DX600, which was intravenously injected and partially relied on blood circulation, corresponding to the distribution of ^{125}I-CoV as follows:

$$\text{Unit uptake of } ^{125}\text{I} - \text{CoV} = 0.95 + 0.77 \times SUV_{ACE2}.$$

$R^2 = 0.152$, $p > 0.05$ (Figure 7E). In other words, unlike the intravenously injected ^{68}Ga-cyc-DX600, in vivo transmission of transocular coronavirus may rely on a more complex pathway that involves the blood circulation system, lymphatic system, interstitial fluid, and so on.

After clarifying the expression of ACE2 in untreated hACE2 mice (Figure 7C), ACE2 PET imaging of the pseudovirus-inoculated hACE2 mice was implemented to assess the association of viral infection with ACE2 expression. Figure 8 presented a pair of typical ACE2 PET images and corresponding quantitative data of hACE2 mice before and at five days P.T. In comparison to the untreated hACE2 mice, ACE2 PET of pseudovirus-inoculated hACE2 mice revealed an infection-related systematic upregulation of ACE2 expression in the organs involved in RAAS (e.g., brain, lung, heart, liver, and kidney) and the organ that was of own local renin–angiotensin-system (e.g., eye). These results revealed that ACE2 expression was upregulated in a short term after infection with CoV.

4 | DISCUSSION

This study successfully established a method that linked virology and diagnosis with molecular imaging. In the methodological view of evaluating the infection efficiency and tracing the infection pathway, GFP or EGFP gene enveloped in pseudovirus is a common way of in vivo tracing.[22] However, the expression of the green fluorescent protein is hard to be dynamically and quantitatively monitored, limited by the weak tissue penetration of fluorescence.

To make the procedure of virus invasion visualized, gamma-emitter nuclides were labeled as pseudovirus, providing an alternative for virus tracing. The following research revealed the in vivo biodistribution of coronavirus via SPECT/CT monitoring. For visual and quantitative analysis, the radioactive signal equaled the distribution of CoV until the obvious de-labeling was detected in the thyroid. In addition to being used for SPECT imaging, I-125 is commonly used in radioimmunoassay, a referable method providing more sensitive information. Specifically for SARS-CoV-2 detection, a rapid detection

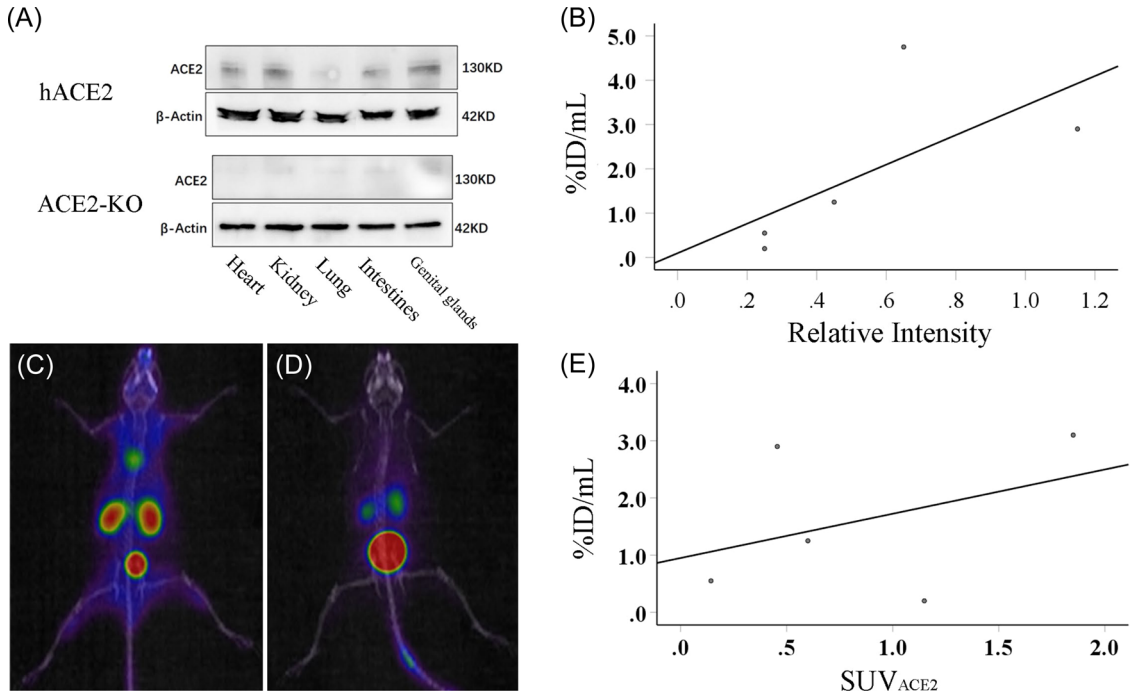

FIGURE 7 Quantification of ACE2 expression with western blot and ^{68}Ga-cyc-DX600 PET, and the corresponding linear relationship with ^{125}I-CoV distribution (as the main metabolic organs, the liver was not included in the linear correlation analysis). (A) The western blot results of hACE2 mice and ACE2-KO mice, and (B) was the linear regression model of ACE2 expression and unit uptake of ^{125}I-CoV; (C, D) ACE2 PET of ACE2 mice and ACE2-KO mice ($n = 3$), and (E) was the linear regression model of SUV_{ACE2} and unit uptake of ^{125}I-CoV. ACE2, angiotensin-converting enzyme; CoV, coronavirus; hACE2, humanized ACE2; KO, knockout; PET, Positron emission tomography; SUV, standardized uptake value.

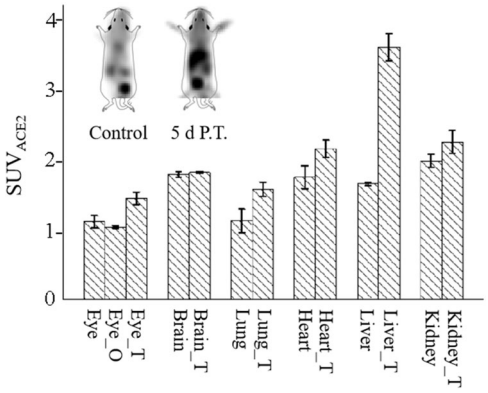

FIGURE 8 ACE2 PET images and corresponding quantitative data of hACE2 mice at 5 days P.T. ($n = 3$, T: treatment; O: opposite). ACE2, angiotensin-converting enzyme 2; hACE2, humanized ACE2; PET, positron emission tomography; P.T., post the treatment; SUV, standardized uptake value.

method has been established using an I-125 labeled spike-specific antibody (^{125}I-CR3022) with a viral concentration as low as 19,700 PFU/mL and as high as 1,970,000 PFU/mL.[23]

^{125}I-CoV SPECT/CT study preliminarily demonstrated that SARS-CoV-2 had a capacity to utilize the eyes as a portal of entry and spread the virus into the body, which was influenced by ACE2 expression in the eye. In fact, the transconjunctival transmission of the virus to respiratory tracts and other tissues has been demonstrated in primates (rhesus monkeys).[24] Our study confirmed this process for the first time by means of virus visualization and further made a quantitative analysis of the corresponding degree of infection, infiltration depth, and virus residue. In quantitative analysis of the transocular path, the lung, and liver were the most concentrated organs of the virus, consistent with a respiratory infection. In addition to the commonly reported respiratory symptoms, SARS-CoV-2 infection of the liver directly manifested the pathological reality of liver damage in patients with SARS-CoV-2.[25]

Notably,^{125}I-CoV SPECT/CT imaging showed that the virus was first distributed to the brain from the start of inoculation to 72 h, and the brain was of a high unit load of coronavirus. This finding allows us to speculate that the brain may be the location where the virus first infects and replicates posttransocular infection. Although several brain radiological imagings have displayed the decreased local brain metabolism or structural changes in the subregion of the brain after infection of SARS-CoV-2,[26,27] intrinsic causative or physio-pathological changes have not been revealed. This study dynamically visualized the process of viral transocular infection via ^{125}I-CoV SPECT/CT, which could provide new insights into neuropsychiatric symptoms ascribed to COVID-19. Also, this study found high and persistent unit virus load in the genital glands and intestines. This finding may help explain some of the symptoms and sequelae observed in long-COVID patients, such as hypogonadism, diarrhea, and nausea.

ACE2-binding affinity has been revealed to be one of the most important factors determining the infectivity of SARS-CoV-2.[19] Since SARS-CoV-2 does not infect conventional laboratory mice,[28] many of the hACE2-transgenic mouse models (e.g., CAG-hACE2 mice) have been developed and employed for assessment and evaluation of vaccine and therapeutic candidates as well as to elucidate basic mechanisms of SARS-CoV-2 infection.[29,30] By employing the CAG-hACE2 mouse model, this study confirmed that SARS-CoV-2 infection is ACE2-dependent and enables short-term upregulation of the cellular receptor ACE2 via molecular imaging of nuclear medicine. This noninvasive and real-time approach may be a powerful complement to existing methods in assessing *ex vivo* isolated samples.[31]

Nevertheless, this survey has some limitations that must be acknowledged. First, as a routine method for virology, the pseudovirus only expresses EGFP at the infected localization after infection, but cannot replicate on its own, what the ^{125}I-CoV SPECT/CT observes is only an initial distribution of the virus. Secondly, due to the small size of the mouse organs, such as the spleen and pancreas, it is technically challenging to measure the radioactive uptake in mice by SPECT/CT. Therefore, the virus distribution in the spleen and pancreas was not evaluated in the present study. Third, the fact that the model mice were under intermittent anesthesia during the early stages of SPECT imaging (i.e., 3–7 h P.T.), may lead to a transient decrease in gastrointestinal function and urinary retention. Finally, in COVID-19-related research, the transgenic mice (e.g., CAG-hACE2 mice, K18-hACE2 mice) that are of distinct promoters or different ACE2 locations are utilized in mimicking hACE2 expression, but there is still a difference in organ connection and organ-specific expression, including the absolute amount and systemic changes. For example, the viral transmission along the optic nerve needs more distance and actuation in humans than in mice. Although the CAG-hACE2 mice are a drawback of widespread cellular expression of hACE2, the Western blot validation is consistent with the human organ-specific amount guaranteed the applicability of the CAG-hACE2 mice model to assess ACE2-dependent viral infection, so as to provide a visual and dynamic overview to better understand the pathogenic process of SARS-CoV-2 infection.

Due to natural selection, the Omicron variant of SARS-CoV-2 has rapidly developed as the predominant circulating strain. Based on the deep learning model, Chen et al.[32] revealed that the Omicron variant (B.1.1.529) was roughly 10 times more infectious than the original virus, and about 2.8 times as infectious as the Delta variant. Recent reports have confirmed that exhaled aerosols from patients with Omicron variant infection contain a large amount of SARS-CoV-2,[33] as well as viral aerosols, survive and maintain their infectious properties for extended periods of time on inanimate surfaces or fomites.[11] The risk of direct or indirect transocular infection with respiratory droplets and virus aerosols cannot be ignored. Overall, the transocular path is common in daily life, and increasing the awareness of eye protection during COVID-19 is necessary. Medical isolation eye masks or face masks are necessary to reduce the infection risk for public and health care workers. For transocular infections, the urinary and digestive systems remain the main excretory routes, proper disposals are also necessary for the cutting of the source of infection.

5 | CONCLUSION

These visual and semiquantitative results are helpful to fully understand the transocular path of SARS-CoV-2 and other coronaviruses. Transocular infection of coronavirus depended on ACE2 expression. The brain, genital glands, and intestines were of the highest unit uptake, potentially accounting for the sequelae. Meantime, lungs and liver were of the highest absolute amount, closely related with the respiratory diffusion and in vivo duplication. Notably, ACE2 expression was upregulated in the short term after infection with SARS-CoV-2.

AUTHOR CONTRIBUTIONS

Danni Li, Liyan Xiong, and Xiao Li were responsible for the conceptualization of the study and chemical synthesis. Liyan Xiong and Tingfang Wang liaised with the Ethics Committee of Shanghai University and obtained ethical approval for the study. Danni Li, Guixia Pan, Rou Li, Lizhi Zhu, Qianqian Tong, Qinqin Yang, and Ye Peng carried out the animal studies, imaging, and ex vivo analysis. Changjing Zuo, Cong Wang, and Xiao Li provided guidance and supervision for the execution of experiments. Danni Li, Guixia Pan, and Xiao Li prepared the draft of the manuscript. All the authors have read and agreed to the final version of the manuscript.

ACKNOWLEDGMENTS

This study was supported by the "Discipline Construction Climbing 234 Plan" of Changhai Hospital of Naval Medical University (Second Military Medical University) (2019YPT002; 2020YPT002); Shanghai Sailing Program (18YF1404100); the National Natural Science Foundation of China (81800349); the Science and Technology Support Project in Biomedical Field of "Science and Technology Innovation Action Plan" of Shanghai Science and Technology Commission (21S21902100); and Shanghai "Rising Stars of Medical Talent" Youth Development Program (SHWRS(2020)_087).

CONFLICT OF INTEREST

The authors declare no conflict of interest.

DATA AVAILABILITY STATEMENT

The data that support the findings of this study are available from the corresponding author upon reasonable request.

REFERENCES

1. Ashraf UM, Abokor AA, Edwards JM, et al. SARS-CoV-2, ACE2 expression, and systemic organ invasion. *Physiol Genomics*. 2021; 53(2):51-60. doi:10.1152/physiolgenomics.00087.2020
2. Hoffmann M, Kleine-Weber H, Schroeder S, et al. SARS-CoV-2 cell entry depends on ACE2 and TMPRSS2 and is blocked by a clinically proven protease inhibitor. *Cell*. 2020;181(2):271-280. doi:10.1016/j.cell.2020.02.052

3. Sato T, Ueha R, Goto T, Yamauchi A, Kondo K, Yamasoba T. Expression of ACE2 and TMPRSS2 proteins in the upper and lower aerodigestive tracts of rats: implications on COVID 19 infections. *Laryngoscope*. 2021;131(3):E932-E939. doi:10.1002/lary.29132
4. Wrapp D, Wang N, Corbett KS, et al. Cryo-EM structure of the 2019-nCoV spike in the prefusion conformation. *Science*. 2020; 367(6483):1260-1263. doi:10.1126/science.abb2507
5. Xia J, Tong J, Liu M, Shen Y, Guo D. Evaluation of coronavirus in tears and conjunctival secretions of patients with SARS-CoV-2 infection. *J Med Virol*. 2020;92(6):589-594. doi:10.1002/jmv.25725
6. Lu C-W, Liu X-F, Jia Z-F. 2019-nCoV transmission through the ocular surface must not be ignored. *Lancet*. 2020;395(10224):e39. doi:10.1016/S0140-6736(20)30313-5
7. Zhou L, Xu Z, Castiglione GM, Soiberman US, Eberhart CG, Duh EJ. ACE2 and TMPRSS2 are expressed on the human ocular surface, suggesting susceptibility to SARS-CoV-2 infection. *Ocul Surf*. 2020;18(4):537-544. doi:10.1016/j.jtos.2020.06.007
8. Coroneo MT, Collignon PJ. SARS-CoV-2: eye protection might be the missing key. *Lancet Microbe*. 2021;2(5):e173-e174. doi:10.1016/S2666-5247(21)00040-9
9. Ocansey S, Abu EK, Abraham CH, et al. Ocular symptoms of SARS-CoV-2: indication of possible ocular transmission or viral shedding. *Ocul Immunol Inflamm*. 2020;28(8):1269-1279. doi:10.1080/09273948.2020.1799035
10. Greenhalgh T, Jimenez JL, Prather KA, Tufekci Z, Fisman D, Schooley R. Ten scientific reasons in support of airborne transmission of SARS-CoV-2. *Lancet*. 2021;397(10285):1603-1605. doi:10.1016/S0140-6736(21)00869-2
11. van Doremalen N, Bushmaker T, Morris DH, et al. Aerosol and surface stability of SARS-CoV-2 as compared with SARS-CoV-1. *N Engl J Med*. 2020;382(16):1564-1567. doi:10.1056/NEJMc2004973
12. Ho D, Low R, Tong L, Gupta V, Veeraraghavan A, Agrawal R. COVID-19 and the ocular surface: A review of transmission and manifestations. *Ocul Immunol Inflamm*. 2020;28(5):726-734. doi:10.1080/09273948.2020.1772313
13. Scialo F, Daniele A, Amato F, et al. ACE2: the major cell entry receptor for SARS-CoV-2. *Lung*. 2020;198(6):867-877. doi:10.1007/s00408-020-00408-4
14. Verma A, Shan Z, Lei B, et al. ACE2 and Ang-(1-7) confer protection against development of diabetic retinopathy. *Mol Ther*. 2012;20(1):28-36. doi:10.1038/mt.2011.155
15. Qiu Y, Shil PK, Zhu P, et al. Angiotensin-converting enzyme 2 (ACE2) activator diminazene aceturate ameliorates endotoxin-induced uveitis in mice. *Invest Ophthalmol Vis Sci*. 2014;55(6):3809-3818. doi:10.1167/iovs.14-13883
16. Foureaux G, Nogueira JC, Nogueira BS, et al. Antiglaucomatous effects of the activation of intrinsic angiotensin-converting enzyme 2. *Invest Ophthalmol Vis Sci*. 2013;54(6):4296-4306. doi:10.1167/iovs.12-11427
17. Li S, Li D, Fang J, et al. SARS-CoV-2 receptor ACE2 is expressed in human conjunctival tissue, especially in diseased conjunctival tissue. *Ocul Surf*. 2021;19:249-251. doi:10.1016/j.jtos.2020.09.010
18. Oz M, Lorke DE, Kabbani N. A comprehensive guide to the pharmacologic regulation of angiotensin converting enzyme 2 (ACE2), the SARS-CoV-2 entry receptor. *Pharmacol Ther*. 2021;221:107750. doi:10.1016/j.pharmthera.2020.107750
19. Beyerstedt S, Casaro EB, Rangel ÉB. COVID-19: angiotensin-converting enzyme 2 (ACE2) expression and tissue susceptibility to SARS-CoV-2 infection. *Eur J Clin Microbiol Infect Dis*. 2021;40(5):905-919. doi:10.1007/s10096-020-04138-6
20. Holappa M, Valjakka J, Vaajanen A. Angiotensin(1-7) and ACE2, "the hot spots" of Renin-Angiotensin system, detected in the human aqueous humor. *Open Ophthalmol J*. 2015;9:28-32. doi:10.2174/1874364101509010028
21. Li X, Li D. A study on an ultra-early PET diagnostic modality for novel coronavirus pneumonia. Compendium of Abstracts of the 2020 Annual Conference of the Nuclear Medicine Branch of the Chinese Medical Association. *J Chin Med Assoc*. 2020:359.
22. Liu SL, Wang ZG, Xie HY, Liu AA, Lamb DC, Pang DW. Single-virus tracking: from imaging methodologies to virological applications. *Chem Rev*. 2020;120(3):1936-1979. doi:10.1021/acs.chemrev.9b00692
23. Pirovano G, Ordonez AA, Jain SK, Reiner T, Carroll LS, Pillarsetty NVK. Rapid detection of SARS-CoV-2 using a radiolabeled antibody. *Nucl Med Biol*. 2021;98-99:69-75. doi:10.1016/j.nucmedbio.2021.05.002
24. Deng W, Bao L, Gao H, et al. Ocular conjunctival inoculation of SARS-CoV-2 can cause mild COVID-19 in rhesus macaques. *Nat Commun*. 2020;11(1):4400. doi:10.1038/s41467-020-18149-6
25. Wang Y, Liu S, Liu H, et al. SARS-CoV-2 infection of the liver directly contributes to hepatic impairment in patients with COVID-19. *J Hepatol*. 2020;73(4):807-816. doi:10.1016/j.jhep.2020.05.002
26. Guedj E, Campion JY, Dudouet P, et al. 18F-FDG brain PET hypometabolism in patients with long COVID. *Eur J Nucl Med Mol Imaging*. 2021;48(9):2823-2833. doi:10.1007/s00259-021-05215-4
27. Douaud G, Lee S, Alfaro-Almagro F, et al. SARS-CoV-2 is associated with changes in brain structure in UK Biobank. *Nature*. 2022;604(7907):697-707. doi:10.1038/s41586-022-04569-5
28. Letko M, Marzi A, Munster V. Functional assessment of cell entry and receptor usage for SARS-CoV-2 and other lineage B betacoronaviruses. *Nat Microbiol*. 2020;5(4):562-569. doi:10.1038/s41564-020-0688-y
29. Jiang W, Shi L, Cai L, et al. A two-adjuvant multiantigen candidate vaccine induces superior protective immune responses against SARS-CoV-2 challenge. *Cell Rep*. 2021;37(11):110112. doi:10.1016/j.celrep.2021.110112
30. Xu G, Li Y, Zhang S, et al. SARS-CoV-2 promotes RIPK1 activation to facilitate viral propagation. *Cell Res*. 2021;31(12):1230-1243. doi:10.1038/s41422-021-00578-7
31. Asaka MN, Utsumi D, Kamada H, et al. Highly susceptible SARS-CoV-2 model in CAG promoter–driven hACE2-transgenic mice. *JCI Insight*. 2021;6(19):e152529. doi:10.1172/jci.insight.152529
32. Chen J, Wang R, Gilby NB, Wei GW. Omicron variant (B.1.1.529): infectivity, vaccine breakthrough, and antibody resistance. *J Chem Inf Model*. 2022;62(2):412-422. doi:10.1021/acs.jcim.1c01451
33. Zheng J, Wang Z, Li J, et al. High amounts of SARS-CoV-2 in aerosols exhaled by patients with Omicron variant infection. *J Infect*. 2022;84(6):e126-e128. doi:10.1016/j.jinf.2022.02.015

How to cite this article: Li D, Xiong L, Pan G, et al. Molecular imaging on ACE2-dependent transocular infection of coronavirus. *J Med Virol*. 2022;94:4878-4889. doi:10.1002/jmv.27958